High-resolution observation of steel using X-ray tomography technique

Toda, Hiroyuki
Department of Mechanical Engineering, Toyohashi University of Technology

Tomizato, Fukuto
Department of Mechanical Engineering, Toyohashi University of Technology

Zeismann, Frank

Motoyashiki-Besel, Yasuko
Institute for Materials Engineering, Kassel University

他

出版情報：ISIJ International. 52 (3), pp.516-521, 2012-03-01
バージョン：
権利関係：

ISIJ International, Vol. 52 (2012), No. 3, pp. 516–521

High-resolution Observation of Steel Using X-ray Tomography Technique

Hiroyuki TODA,[1)] Fukuto TOMIZATO,[1)] Frank ZEISMANN,[2)] Yasuko MOTOYASHIKI-BESEL,[2)] Kentaro UESUGI,[3)] Akihisa TAKEUCHI,[3)] Yoshio SUZUKI,[3)] Masakazu KOBAYASHI[1)] and Angelika BRUECKNER-FOIT[2)]

1) Department of Mechanical Engineering, Toyohashi University of Technology, Toyohashi, Aichi, 441-8580 Japan. E-mail: toda@me.tut.ac.jp, tomizato@four-d.me.tut.ac.jp, m-kobayashi@me.tut.ac.jp 2) Institute for Materials Engineering, Kassel University, Moenchebergstrasse 3, D-34125 Kassel Germany. E-mail: zeismann@uni-kassel.de, besel@uni-kassel.de, a.brueckner-foit@uni-kassel.de 3) Japan Synchrotron Radiation Research Institute, 1-1-1, Kouto, Mikazuki-cho, Sayo-gun, Hyogo, 679-5198 Japan. E-mail: ueken@spring8.or.jp, take@spring8.or.jp, yoshio@spring8.or.jp

(*Received on May 30, 2011; accepted on October 19, 2011*)

A common, serviceable form of steel has been observed by employing synchrotron X-ray microtomography technique. Spatial resolution has been optimized using a test object with varying experimental conditions. Reasonably high resolution, which is close to the theoretical upper limit for the projection-type X-ray tomography, has been achieved for a reasonably large specimen. Its application has made it possible to clearly observe a fatigue crack and its opening behavior in steel, and to demonstrate some quantitative mechanical evaluations.

KEY WORDS: microtomography; synchrotron radiation; spatial resolution; crack; dual phase steel.

1. Introduction

Over the past decade, attempts have been made to apply synchrotron X-ray microtomography (XMT) to ferrous materials, as the importance of 3D observation has been recognized. XMT performed on light materials has generally enabled the reconstruction of volumes with maximum spatial resolution close to the physical limit of the projection-type set-up (approximately 1 μm).[1,2)] However, in the case of ferrous materials, difficulties arise with respect to X-ray transmission. Since photoelectric absorption is dramatically enhanced with increasing atomic number, high energy X-rays are needed to realize X-ray imaging for ferrous materials. This can lead to spatial resolution degradation, in addition to image quality degradation due to poor photon statistics. For example, Everette *et al*. and Lame *et al*. have utilized white X-rays to observe steel at a spatial resolution of 3 and 2.7 (not on ferrous materials, but on Cu) μm, respectively.[3,4)] Cheong *et al*. (90 keV X-ray was used for field of view of 4.34 mm) and Shobu *et al*. (66.4 keV X-ray was used for field of view of 5.97 mm) used monochromatic X-rays from undulators;[5,6)] and although no measurement or description of spatial resolution is presented in their papers, spatial resolutions of 19 and 35 μm, respectively, are expected at best, according to the descriptions of sample size and the number of projections. This technological limitation prevents us from utilizing advanced applications of XMT, such as measurements of 3D/4D crack-tip displacement/strain fields,[7)] local crack driving forces,[8)] and the spatial distribution of chemical concentrations,[9)] which have been developed mainly using light materials.

It would therefore be of significant value to attain the best achievable spatial resolution level for ferrous materials. In the present study, an XMT study was performed at a synchrotron radiation facility to examine the effects of various experimental parameters on spatial resolution. Fatigue crack opening behaviors were then evaluated, and advanced analysis performed, by applying the optimal experimental conditions obtained.

2. Spatial Resolution Evaluation

2.1. X-ray Tomography Experiments

XMT was performed at the undulator beamline BL20XU of the SPring-8. A monochromatic X-ray beam, produced by a liquid nitrogen-cooled Si (511)–(333) double crystal monochromator, was used. The image detector consisted of a cooled 4 000 (H) × 2 624 (V) element CCD camera (pixel size of the camera: 5.9 μm square) in 2 × 2 binning mode, a scintillator (Lu_2SiO_5:Ce), and an optical microscope objective lens (×20). Thickness of the LSO scintilllator was 10 and 26 μm for 40 and 55/70 keV, respectively. In total, 1 500 radiographs, scanning 180 degrees, were obtained in 0.12-degree increments. As mentioned above, the theoretical limit of the projection-type XMT is approximately 1 μm, which is determined primarily by inevitable image blurring caused by Fresnel diffraction, the diffraction limit of visible light, and the spatial resolution of a scintillator.[10)] Isotropic voxels (a volume element in 3D space) with 0.5 μm edges, that were requisite to achieve the 1 μm spatial resolution, were achieved in the reconstructed slices.

In order to realize high-resolution imaging for ferrous materials, high photon energies of 40–70 keV were used in this study. Thermal stability of the monocromator is crucial

for maximizing beamline stability. Recently, the cooling system of the cryogenically cooled monochromator has been substantially improved in the SPring-8,[11] enabling the use of almost full photon flux at the high X-ray energies required for the XMT experiments on ferrous materials. In addition, in order to obtain high X-ray flux, the beam diffuser usually employed to modify the high coherence of low to intermediate energy X-rays was removed from the set-up.

2.2. Spatial Resolution Evaluation

The first purpose of this study was to optimize the spatial resolution of the XMT set-up at high X-ray energies, by varying experimental parameters. Test patterns were designed to test spatial resolution. The test patterns consisted of pairs of lateral and vertical gratings with increasing line pitch between 1.36–2.65 μm and 1.32–2.47 μm, respectively, as shown in **Fig. 1**. The test patterns were machined on a stainless-steel wire of about 497 μm in diameter using the focused ion beam milling technique. Since stainless steel has no visible microstructure with the present imaging set-up, it may be assumed to be an ideal substrate material. The modulation transfer function (MTF) derived from an edge response function (ERF) at the outer contour of the wire (*i.e.*, the steel/air interface) was also measured, to determine the spatial resolution at 5% contrast ratio. This measurement corresponds to the lateral direction, which is the circumferential direction with respect to the stainless-steel wire axis.

The test-pattern wire was scanned at 40, 55 and 70 keV, with varying sample/detector distance. The results of the interface-based MTF calculations and the subjective inspection of the test patterns suggested fundamentally reasonable agreement. **Figure 2** shows examples of virtual cross-sections captured at a sample/detector distance of 110 mm. Even the narrowest grating was resolved with each of the three X-ray energies used. The variations in lateral (radial

Fig. 1. A resolution test object that has been prepared on a stainless-steel wire of about 497 μm in diameter using the focused ion beam technique. The three arrows indicate three directions along which spatial resolution was measured.

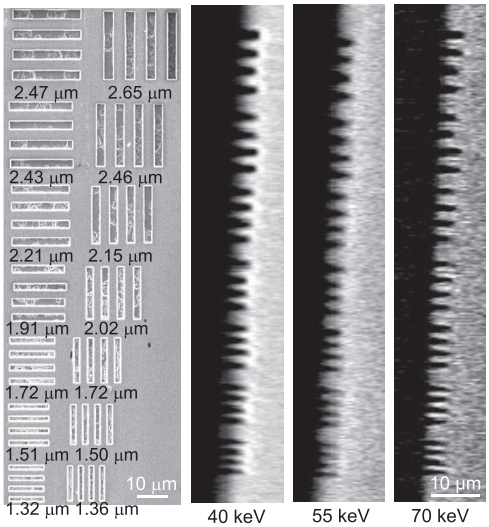

(a) Line pairs (Scanning ion microscopy image) (b) Virtual cross sections (Microtomography image)

Fig. 2. Examples of virtual cross-sections captured at sample/detector distance of 110 mm, showing how the lateral gratings for vertical resolution evaluation can be resolved at the three X-ray energies. Note that even the narrowest grating was resolved with the three X-ray energies used.

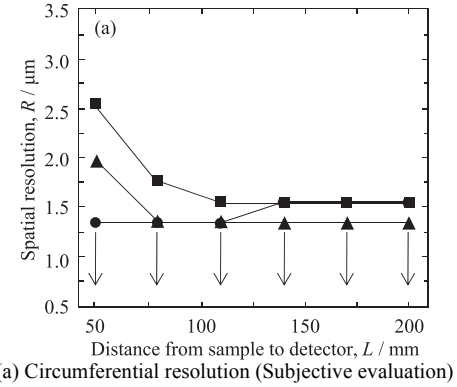

(a) Circumferential resolution (Subjective evaluation)

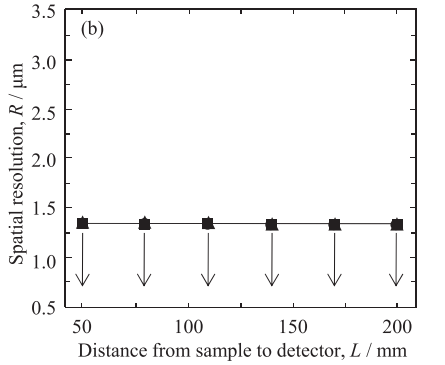

(b) Vertical resolution (Subjective evaluation)

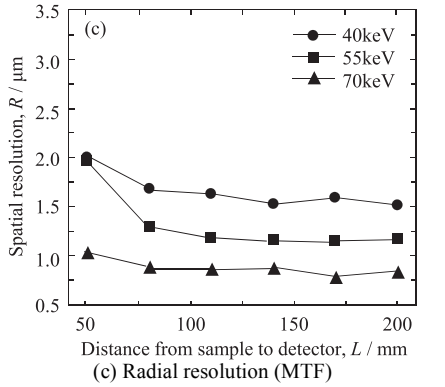

(c) Radial resolution (MTF)

Fig. 3. Variation in spatial resolution in (a) lateral (circumferential), (b) vertical and (c) lateral (radial) directions with respect to the rotation axis. (a) and (b) were obtained through subjective evaluation of the resolution test object, while (c) was determined with MTFs derived from ERFs at the outer contour of the wire. Spatial resolution was defined at modulation transfer function of 5%. Original line spread functions were fitted with a sigmoid function.

with respect to the stainless-steel wire axis) and vertical resolution with sample/detector distance are shown in **Figs. 3**(a) and 3(b), respectively. It can be confirmed that the vertical resolution exceeds the lateral resolution, at least at 55 and 70 keV. The lateral resolution results further reveal that spatial resolution worsens when the sample is closer to the detector. This is probably due to the effects of X-ray scattering. It is well known that at a relatively low X-ray energy range (~ 20 keV) the X-ray scattering distribution is approximately isotropic, while increasing the X-ray energy causes a preferential forward scattering.[12] The X-ray photons that are forward directed are more apt to be detected by the image detector when the sample/detector distance is small, thereby reducing spatial resolution.

Figure 4 shows edge response functions revealing the degree of blurring across the sharp air/steel interface. Obvious overshoot and undershoot may be observed in the profiles. Since these are caused by X-ray refraction at the interface, the extent of the overshoot and undershoot increases with the increase in distance. Furthermore, it is qualitatively evident that spatial resolution is not significantly different among the three conditions. A total of eight measurements were averaged for each ERF. A line spread function (LSF) was obtained by taking the first derivative from each ERF that had been fitted with a sigmoid function. MTF was then derived by applying discrete Fourier transform to the LSF.

Figure 3(c) shows the variations in lateral (circumferential with respect to the stainless-steel wire axis) direction with respect to the spatial resolution that were obtained by means of MTF. Although the lateral resolution appears to differ between Figs. 3(b) and 3(c), it should be noted that the measuring directions differ between Figs. 3 (b) (circumferential direction) and 3(c) (radial direction) with respect to the stainless-steel wire axis. Comparisons of all the resolution data shown in Fig. 3 indicate that the spatial resolution is unexpectedly highest in all three directions when the X-ray energy is 70 keV. This may be associated with the characteristics of the Lutetium-based scintillator employed. The size of the volume in the scintillator in which X-rays are absorbed and scintillation photons are produced is generally dependent on the X-ray energy. If this volume is less than the diffraction-limited resolution of the optical system used, the spatial resolution of the system is not limited by the X-ray absorption process. It is however reasonable to assume that the absorption mean free path of X-ray radiation depends on photon energy at high X-ray energies. Hence, it may be assumed that the lower the photon energy is, the better the resolution achieved in the image. This is because the spreading of the visible photons produced in the scintillator acts to blur the image. It is however interesting to note that Lu has K absorption edge at 63.314 keV, and this inevitably causes the smallest absorption mean free path at 70 keV among the three X-ray energies employed, thereby resulting in beneficial effects on spatial resolution.

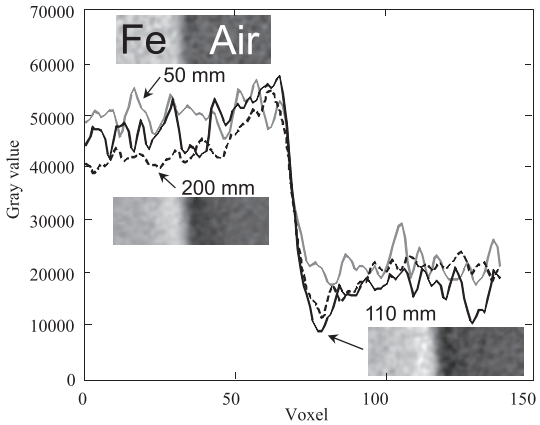

Fig. 4. Examples of ERFs (which indicate how original images are spread out), used to calculate MTFs of 3D images. X-ray energy was 55 keV for these examples.

3. Application to 4D Observation of a Cracked Medium

3.1. Experimental Details

The material used in this section was S15C carbon steel, which exhibits a ferritic-martensitic structure with comparatively large areas of martensite due to a special heat treatment. The alloy used had a chemical composition of 0.15 C, 0.15 Si, 0.41 Mn, 0.014 P, 0.008 S and balance Fe in mass%. A specimen of 22 mm (length: L) × 0.475 mm (width: W) × 0.481 mm (thickness: B) with a corner fatigue crack was prepared in the form of an I-shaped specimen. The values of W and B are within a 0.6 mm long gauge length. The fatigue pre-crack was introduced at room temperature in air, using a servohydraulic fatigue-testing machine, applying sinusoidal loading with a load ratio P_{min}/P_{max} of 0.1 and maximum stress of 350 MPa.

A photon energy of 40 keV and sample/detector distance of 110 mm were adopted as a result of the spatial resolution evaluation described in section 2.2. The other details are the same as in the previous section. The entire cross-section of the specimen, and a region about 650 μm high containing the crack, were captured on the CCD camera. An in-situ loading rig, which had been specially designed for the in-situ XMT observation, allowed specimens to be scanned under cyclic loading. The test rig controller had a load resolution of 0.1 N, which made it possible to undertake well-controlled material tests using the miniaturized specimen. The test rig exhibited a displacement stability of about 0.1–0.2 μm, thereby enabling the production of tomographic scans with almost no blurring caused by specimen wobble. All the scans were performed while the loaded samples were being held at fixed displacements. Each view required 0.3 s to acquire the image, and each full tomographic scan required about 22 min. A first scan of the tomography was performed without loading (2.4 N). Subsequent scans were performed at 6.7, 13.4, 20.2, 26.9, 33.6 and 60.0 N, after the relaxation behavior of the material was stabilized. Image slices were reconstructed from the series of projections, based on a conventional filtered back-projection algorithm.[13] The gray value in each dataset was calibrated so that the linear absorption coefficient of 3–50 cm^{-1} fell within an 8-bit gray scale range between 0 and 255.

3.2. Local Strain and CTOD Measurement Methods

Particles such as carbides and pores observed in the tomographic volumes were segmented and labeled. To calculate the gravity center of each particle and pore with sub-voxel accuracy, pentagonal facetted iso-intensity surfaces were computed from the volumetric data set using the conven-

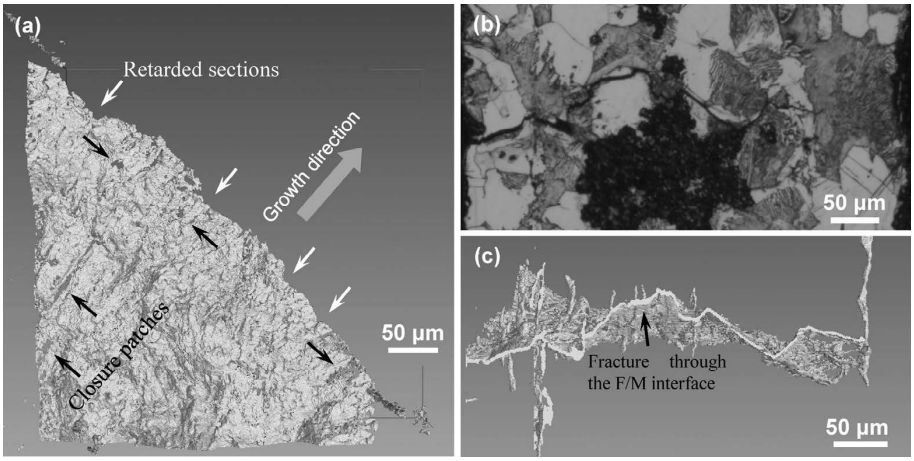

Fig. 5. 3D perspective views of a fatigue crack. Only crack images have been extracted from the tomographic volume and shown in (a) and (c), while the underlying metal and other microstructural features are not displayed. The crack is viewed in the mode I loading direction in (a) and the crack mouth direction in (c). (b) is an optical microscope image that corresponds to (c).

tional marching cubes algorithm.[14] To suppress inaccuracies originating from image noise, only particles over 27 voxels in volume were counted for particle tracking. Volume, V, surface area, A, and the center of gravity were measured in the tomographic images. Precise image registration was then performed before the particles were tracked using a transformation matrix that minimizes the sum of the distances between identical particles captured at neighboring scan steps. The particles were tracked throughout the tensile loading by employing a matching probability parameter (MPP) method with local pattern matching, called the modified spring model, which we had previously developed.[15,16] The optimal values of coefficients α, β and γ in the MPP were identified as 0.8, 0.1 and 0.1, respectively, in preliminary analysis for the material used. To increase both the success ratio and the number of particles tracked, a trajectory prediction[16] was also applied, in order to track particles in conjunction with the MPP and modified spring methods. Tetrahedra with all the particles and pores as vertices in the 3D image were created by the Delaunay tessellation technique, which generates an aggregate of space-filling irregular tetrahedra,[17] to calculate internal strain in 3D in high density.[16] All the strain components were calculated from the displacement of the vertices of the tetrahedrons, assuming that the displacement in a given tetrahedron is a linear function. Crack-tip opening displacement (CTOD) was also measured on each slice. The process for measuring CTOD and COD variation is described elsewhere.[8]

3.3. Evaluation of Obtained XMT Images

Owing to the superior spatial resolution level attained, both cracks and some microstructural features of the underlying steel could be clearly visualized. In total, 1 249 dispersion particles and 1 687 micropores were confirmed in the entire rendered volume. The particle volume fraction was 0.04% and the mean equivalent diameter was 4.3 μm, while those for the micropores were 0.11% and 5.4 μm, respectively, for the volume shown in **Fig. 5**. As mentioned above, the particles and pores are limited to those larger than 27 voxels in volume. It may be inferred that the number of visible microstructural features is somehow enough to derive

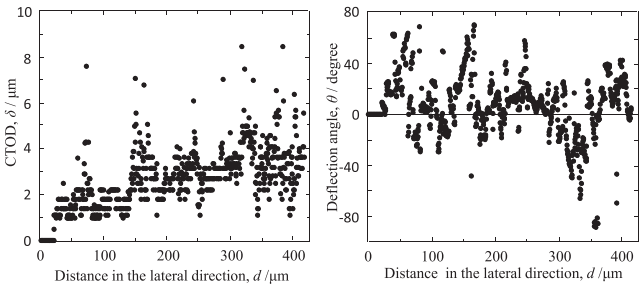

(a) Crack tip opening displacement (b) Deflection angle

Fig. 6. The distribution of CTOD along the crack front line in (a) and corresponding deflection angle distribution in (b).

various internal mechanical quantities such as stress/strain and local crack driving forces. In Fig. 5, only crack images were extracted from the tomographic volume captured at 2.4 N, and the underlying metal and other microstructural features are not displayed. They are shown as 3D perspective images viewed in the mode I loading direction in Fig. 5(a) and the crack mouth direction in Fig. 5(c). Figure 5(b) is an optical microscope image that corresponds to Fig. 5(c). Figure 5(a) reveals the distribution of some fatigue crack closure patches (indicated by black arrows), that don't completely disappear even at relatively high load levels. It has been well documented in the literature that such scattered closure patches contribute effectively to fatigue crack growth resistance.[18,19]

Crack extension varied to some extent along the crack front line. A few retarded sections of the crack front are seen periodically, as indicated by white arrows in Fig. 5(a), together with some fracture surface roughness. Other noteworthy features are the significant crack deflection and tilting caused by the occurrence of modes II and III driving forces, respectively, which can be more obviously identified in Fig. 5(c). In fact, the underlying phases have been identified, as shown in Fig. 5(b), as the ductile ferrite phase and the less ductile martensite phase,[20] which can be associated with the significant mode III tilting shown in Fig. 5(c). Frequent changes in tilting direction are confirmed at martensite/ferrite interfaces, together with some martensite/ferrite interfacial crack extension where the crack front line

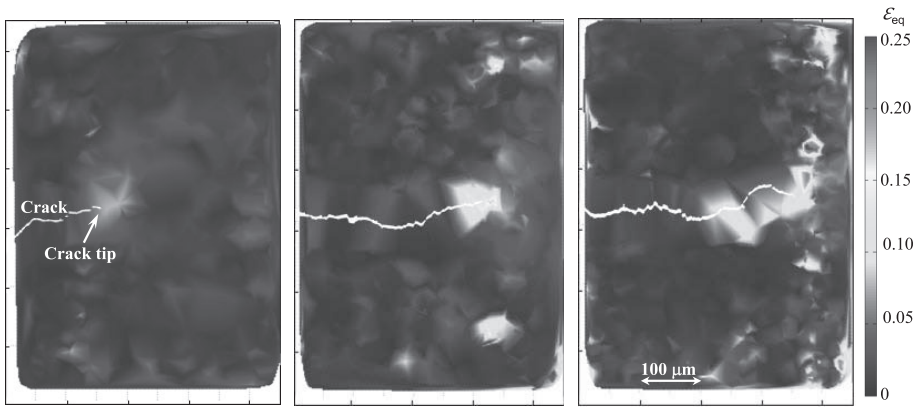

(a) 125 μm in lateral distance (b) 300 μm in lateral distance (c) 350 μm in lateral distance

Fig. 7. The examples of crack-tip strain field shown on three different virtual cross-sections. Equivalent strain is shown in the figure.

becomes more complicated. A typical example is indicated by the arrows in Figs. 5(b) and 5(c). It can be inferred that the retarded sections of the crack front might be associated with the existence of the martensite grains.

3.4. Quantitative Assessments of Crack Extension Behavior

Figure 6(a) shows the variations in measured CTOD along the crack front line at an applied load of 60 N. The CTOD value tends to roughly increase when going from left to right. It appears to increase locally four to five times over intervals of approximately 10 to 50 μm along the crack front line, probably because of the crack/microstructure interaction that was shown in Fig. 5. This is because the length range over which the CTOD values are locally elevated corresponds to the dimensions of the ferrite/martensite grains that are shown in Fig. 5(b). The local CTOD elevation can also be associated with the occurrence of local crack deflection shown in Fig. 6(b), providing evidence for the effects of the underlying grain dual phase structure.

Figure 7 shows examples of crack-tip strain field shown on three different virtual cross-sections that has been calculated between applied loads of 33.6–60.0 N. It is clear that the strain distribution is far different from that obtained in typical elastic-plastic fracture mechanics. Although the measurement does not provide an exceedingly high spatial density in displacement markers, due to the relatively small number of microstructural features visible that can be utilized as strain markers, it appears most likely that the strain distribution has been affected significantly by the underlying microstructure. Figure 7 also shows how the crack-tip strain field varies from place to place. In Fig. 7(c), vertical elongation of the crack-tip strain field is observed in both upper and lower directions. This characteristic geometry of the crack-tip strain field can be associated with the existence of considerably elongated inclusion particles in the vicinity of the crack-tip. Such particles can be clearly recognized in Fig. 5(c) as ten to twelve needle-like inclusions that align in the vertical direction.

6. Summary

X-ray microtomography was employed to observe a fatigue crack and microstructural features in S15C steel. A high-resolution experimental configuration enabled surprisingly superior spatial resolution of better than 1.3 μm after optimizing experimental parameters. The specimen size employed in the present study was comparable to that used in similar experiments on lighter materials such as aluminum, whose results have been reported in recent literature. The spatial resolution level achieved in the present study is clearly advantageous compared to the limited past trials on ferrous materials. Owing to the high spatial resolution achieved, the details of a crack were readily observed, along with evidence of the interaction between the crack and a dual phase microstructure. After preliminary investigation of the obtained images, two kinds of measurement methods, previously developed by the present authors, were used to quantify crack-tip opening displacement and crack-tip strain, and provided evidence of microstructure/crack interactions.

It may be concluded that the use of 4D microtomography observation, combined with advanced image-analysis techniques, might offer a highly effective means of investigating various issues relating to ferrous materials. The high-resolution microtomography observation achieved in the present study is of crucial importance to the development and application of such techniques.

Acknowledgements

This work was partly undertaken as a technical research aid project of the JFE 21st Century Foundation awarded to HT. The synchrotron radiation experiment was performed with the approval of JASRI through proposal number 2010A1247 (Project leader: YMB).

REFERENCES

1) H. Toda, K. Shimizu, K. Uesugi, Y. Suzuki and M. Kobayashi: *Mater. Trans.*, **51** (2010), 2045.
2) H. Toda, T. Hidaka, M. Kobayashi, K. Uesugi, A. Takeuchi and K. Horikawa: *Acta Mater.*, **57** (2009), 2277.
3) R. K. Everett, K. E. Simmonds and A. B. Geltmacher: *Scr. Mater.*, **44** (2001), 165.
4) O. Lame, D. Bellet, M. Di Michiel and D. Bouvard: *Acta Mater.*, **52** (2004), 977.
5) K. S. Cheong, K. J. Stevens, Y. Suzuki, K. Uesugi and A. Takeuchi: *Mater. Sci. Eng. A*, **513–514** (2009), 222.
6) T. Shobu, K. Tanaka, A. Hashimoto and J. Narita: *J. Soc. Mater. Sci. Jpn.*, **58** (2009), 588.
7) L. Qian, H. Toda, K. Uesugi, M. Kobayashi and T. Kobayashi: *Phys. Rev. Lett.*, **100** (2008), 115505.
8) H. Toda, S. Yamamoto, M. Kobayashi and K. Uesugi: *Acta Mater.*,

56 (2008), 6027.
9) H. Toda, T. Nishimura, K. Uesugi, Y. Suzuki and M. Kobayashi: *Acta Mater.*, **58** (2010), 2014.
10) A. Tekeuchi, K. Uesugi, H. Takano and Y. Suzuki: *Rev. Sci. Instru.*, **73** (2002), 4246.
11) SPring-8 Annual Report, BL20XU, SPring-8, Hyogo, (2007), 77.
12) J. A. Seibert and J. M. Boone: *J. Nuc. Med. Tech.*, **33** (2005), 3.
13) G. T. Herman: Image reconstruction from projections, Academic Press, San Francisco, (1980), 1.
14) W. E. Lorensen and H. E. Cline: *Comput Graph (ACM).*, **21** (1987), 163.
15) M. Kobayashi, H. Toda, Y. Kawai, T. Ohgaki, K. Uesugi, D. S. Wilkinson, T. Kobayashi, Y. Aoki and M. Nakazawa: *Acta Mater.*, **56** (2008), 2167.
16) H. Toda, E. Maire, Y. Aoki and M. Kobayashi: *J. Strain Anal. Eng. Design.*, **46** (2011), 549.
17) C. B. Barber, D. P. Dobkin and H. T. Huhdanpaa: *ACM Trans. Math. Soft.*, **22** (1996), 469.
18) H. Toda, I. Sinclair, J. Y. Buffière, E. Maire, T. Connolley and M. Joyce: *Philos. Mag. A.*, **83** (2003), 2429.
19) H. Toda, I. Sinclair, J. Y. Buffière, E. Maire, K. H. Khor and P. Gregson: *Acta Mater.*, **52** (2004), 1305.
20) Y. Motoyashiki, A. Bruckner-Foit and A. Sugeta: *Fatigue Fract. Eng. Mater. Struct.*, **30** (2007), 556.